Insights into the interaction of a shale with CO_2

Eleni Stavropoulou[1,*] and Lyesse Laloui[1]

[1]Ecole Polytechnique Fédérale de Lausanne (EPFL), Laboratory for Soil Mechanics

(LMS), EPFL-ENAC-LMS, Station 18, CH-1015 Lausanne, Switzerland

[*]eleni.stavropoulou@epfl.ch

Abstract

Caprock formations such as shales, play a key role to safe underground CO_2 storage since they serve as a hydromechanical barrier that prevents migration of the injected CO_2 to the surface. While their hydromechanical response is important to ensure their sealing capacity, interaction with the injected CO_2 involves additional thermo-chemo-mechanical (THMC) phenomena that may threaten the long-term caprock's integrity. The low transport properties of shales make them a suitable caprock material, but at the same time challenging to study due to the very long time scales that are required for the various thermo-hydro-chemo-mechanical processes to manifest. In this work, the multiphysical interaction of the Opalinus Clay shale with CO_2 is studied with live x-ray tomography. Long-term exposure to liquid and supercritical CO_2 targets the investigation of different occurring THMC processes locally and globally in 3D that are often indistinguishable with conventional lab testing protocols. To improve spatial and temporal resolution while applying realistic pressure and temperature conditions, small size samples are studied. Long-term injection of liquid CO_2 resulted to a siginificant fissuring of calcite-rich zones that were for the first time visualised and quantified from the x-ray images, while a re-arrangement of the pre-existing micro-fissures in the clay matrix were observed. The volumetric response during direct exposure of an Opalinus Clay sample to supercritical CO_2 revealed an initial swelling at pre-cracked zones and initiation of new micro-fissures at areas of direct contact with the anhydrous CO_2 due to pore

24 water evaporation. Advanced 3D image analysis showed an increasing CO_2 uptake ~~with time the~~

25 elevated value of which after pressure release suggests potential CO_2 trapping the material.

1 Introduction

27 Geological CO_2 Storage (GCS) is an efficient way to permanently store large volumes of captured

28 CO_2 by subsurface injection at pressures higher than its critical ~~phase point~~ (P_{cr} = 7.4 MPa) where

29 it changes from gaseous to liquid state and above a certain temperature level (T_{cr} = 31.2°C) to su-

30 percritical. This relatively high pressure level strongly encourages the selection of deep reservoirs

31 (min. 700-800 m depth), where the *in-situ* water/brine pressure equilibrates the injected CO_2 pres-

32 sure. According to the most recent IPCC report (IPCC, 2022), Carbon Capture and Storage (CCS) is

33 key to reaching net-zero emissions by mid-century and mitigating climate change. Besides, the need

34 to implement CCS in a range of sectors including energy production, manufacturing and industry is

35 underlined in the same report.

36 The feasibility of the technology relies on successful long-term subsurface storage which depends

37 – at least during the first few decades – on the performance of nearly impermeable geological for-

38 mations (seal/caprock) that will prevent CO_2 migration to the surface. Caprock formations, typically

39 shales or tight mudrocks, are highly heterogeneous with low mass transfer properties, and their prone

40 response to Thermo-Hydro-Chemo-Mechanical (THMC) loads remains a complex subject that de-

41 serves further inquiry.

42 Shales have been studied since decades by the oil and gas industry, more recently for their use as

43 geological barriers for nuclear waste storage, but full understanding of their suitability for geological

44 CO_2 storage is still somewhat limited, since CO_2 injection further complexifies an already difficult

45 engineering problem: (i) Unlike oil or water, CO_2 diffusion results in acidification of the *in-situ* brine

46 that can lead to chemical interactions in the caprock and alteration of its mechanical and transport

47 properties (Yang *et al.*, 2022); (ii) CO_2 injection introduces stress state changes in both the reservoir

48 and the overlaying caprock that can cause reactivation of pre-existing faults or creation of new fracture

49 systems (Vilarrasa *et al.*, 2019).

50 Significant progress in experimental data collection has been achieved in various scales (Armitage

51 *et al.*, 2010; Houben *et al.*, 2013), related to both geomechanical response (Rutqvist, 2012; Wang and

52 Tokunaga, 2015; Kivi *et al.*, 2022) and chemical interactions (Wollenweber *et al.*, 2010; Hadian and

53 Rezaee, 2020) during exposure to CO_2-rich fluids. Shales are anisotropic and highly heterogeneous

54 at different scales (micro to macro) with strong geomechanical and geochemical couplings that often

55 challenge our ability to distinguish the different occurring phenomena and estimate their time-scale

56 during CO_2 exposure.

57 In recent years, the Opalinus Clay shale has been studied as a potential caprock in the context of

58 geological CO_2 storage (Amann *et al.*, 2013; Favero *et al.*, 2016; Makhnenko *et al.*, 2017; Sciandra *et

59 al.*, 2021), thanks to favourable properties such as low porosity (< 20%), low permeability (in the order

60 of 10^{-20} m^2), high clay content (40-80%), swelling properties and high sealing capacity (Marschall

61 *et al.*, 2005; Crisci *et al.*, 2019; Delage and Belmokhtar, 2022). These favourable properties of

62 Opalinus Clay (and shales more generally) make it a challenging material to study due to the slow

63 flow processes at resolutions that may fall within the measurement error (Minardi *et al.*, 2021).

64 Representative testing of shales remains a big issue. Representative boundaries do not only in-

65 volve applied pressure or temperature but also the spatial and temporal scale of the measurement.

66 While large scale experiments are generally considered to be more realistic, they can be challenging

67 to properly monitor and analyse since they involve the combination of multiple phenomena occurring

68 under different scales, in particular in heterogeneous materials such as shales. A real scale exper-

69 imental campaign has been recently completed at the Underground Research Laboratory (URL) in

70 Mont Terri, where CO_2-rich brine has been injected in an existing fault in Opalinus Clay (Zappone

71 *et al.*, 2021). The results have not been conclusive, given the low applied pressure, the volume of

72 injected CO_2 and the long time-duration required for transport phenomena to manifest in that scale.

73 In parallel, recent lab-scale experimental results from CO_2 injection tests in Opalinus samples do not

74 show evidence of significant influence on the material's basic properties for the given test duration

75 (Minardi *et al.*, 2021; Favero & Laloui, 2018); grain density, dominant entrance pore size and void

76 ratio, as well as hydraulic conductivity do not vary in a considerable way after exposure to CO_2 over

77 a weekly time-scale. The short duration of these tests together with the chosen sample size could be

78 among the reasons for the absence of measurable evolution.

79 Representative testing conditions and duration are even more challenging when processes of geo-

80 chemical nature are investigated. Indeed, the impact of chemical reactivity of shales in the presence

of CO_2 remains a very challenging topic. While shales contain minerals reactive to CO_2, current lab measurements are not enough since they rely either on *post-mortem* analysis of fluid composition or mineralogy (Armitage *et al.*, 2013; Elkady and Kovscek, 2020). The indirect interpretation of permeability results before and after CO_2 exposure in terms of chemical alterations (dissolution/precipitation) can be ambiguous since they may involve self-compensating mechanisms such as carbonate dissolution, mechanical crushing and inelastic compaction as shown by various authors who studied fractured caprock samples (Yasuhara *et al.*, 2011; Hashemi and Zoback, 2021). It is thus difficult to build solid conclusions on their impact on the structural properties of the material and hence transport and mechanical response.

Taking all the above into account, there is a series of issues when testing shales in the context of CO_2 storage: (i) Flow is extremely slow resulting in long testing durations; (ii) Measured permeability variations are close to the measurement error; (iii) Reproduction of real site conditions is crucial since injection pressure and therefore effective stress has an important impact on properties of the material that drive flow and breakthrough, *i.e.* connected porosity; (iv) Chemical interactions are limited by the slow transport properties (v) The testing duration and scale that are commonly used are not enough to allow investigation in that direction.

In this work, the different coupled processes and phenomena that occur when CO_2 interacts with a shaly caprock material – the Opalinus Clay – are explored based on a series of measurements and observations from *real time* x-ray tomography. Taking full advantage of this non destructive tool, new aspects and results are targeted and demonstrated that aim to improve our understanding of the caprock's response while under realistic testing conditions. The originality of the presented research relies on the study of smaller size samples where observation period is expected to be shorter, and most importantly the direct measurement of strain fields and structural alteration from the analysis of the 3D tomographic images. In the following, the proposed methodology, tools and analysis conventions are presented in detail. The results of two experimental campaigns where Opalinus Clay shale is exposed to either liquid or supercritical CO_2 are presented and discussed. These experiments target different coupled mechanisms that combined aim to contribute to a more profound understanding of the overall THMC response of shales with CO_2.

2 Methodology, Tools and Analysis Principles

Shales are highly heterogeneous and anisotropic materials, sensitive to thermo-hydro-mechanical variations and with strong multiphysical couplings and very slow transport properties (Mohajerani *et al.*, 2014; Favero *et al.*, 2016; Menaceur *et al.*, 2016; Li and Laloui, 2017). Inevitably, representative testing of shales requires the employment of methods and tools that can embrace these particularities by means of controlled applied conditions and *full-field* measurement, *i.e.* a field record of a quantity (*e.g.*, deformation, density, temperature, *etc.*) as opposed to point-wise data (Viggiani and Hall, 2008).

Taking into account all the above, the exploration of a new approach in testing shales with *in-situ* x-ray tomography is motivated. In this study, the full-field of micro-structural variations and kinematics of the Opalinus Clay shale when exposed to CO_2 under different boundary conditions are targeted with 3D image analysis of real-time x-ray tomographies. Long-duration exposure of Opalinus Clay to injected liquid CO_2 (8 MPa) under confined conditions (10 MPa) aims to reveal potential chemomechanical processes, while direct exposure of unjacketed Opalinus Clay to supercritical CO_2 targets the better understanding of localised THM interactions that are otherwise difficult to detect with conventional lab-testing techniques.

Despite the classic testing approaches on centimetric size shale samples in the literature, in this work very small samples (5 mm) are studied in order to first gain in temporal resolution (partly inspired by small-scale permeability testing equipment (Birmpilis *et al.*, 2019; Birmpilis and Dijkstra, 2021), but also to optimise the quality of x-ray imaging (improved spatial resolution). This approach is challenging for the given material and the given subject; the pore size of shales is in the order of nanometres and thus impossible to visualise with x-ray micro-tomography (micrometric scale). Nonetheless, observation and quantification of microstructural modifications due to CO_2 can be explored with relatively high scanning resolutions (5-8 μm/px) and fast tomographies thanks to the small size of the sample.

2.1 *In-situ* x-ray micro-tomography and experimental protocol

A few authors have investigated the heterogeneity and anisotropic behaviour of shales pointing out the role of the microstructure by employing different imaging techniques (Wang *et al.*, 2013; Desbois

137 *et al.*, 2017; Delage & Tessier, 2021). In the case of experimental geomechanics, x-ray tomography

138 is the most widely used technique, with a large range of results stated in literature (Viggiani *et al.*,

139 2015; Bedford *et al.*, 2017; Vego *et al.*, 2022; Birmpilis *et al.*, 2022). The great advantage of x-

140 ray tomography compared to other techniques for soil characterisation (*e.g.* SEM microscopy), is

141 the possibility to identify in 3D the specimen's heterogeneity and follow its evolution in time (*in-situ*

142 testing). This is a very powerful tool that allows a better interpretation of test results, such as measured

143 permeability, fingering phenomena, localised deformation or structural modifications (Voltolini and

144 Ajo-Franklin, 2020; Stavropoulou *et al.*, 2020).

145   For this study, the dual x-ray source in PIXE platform (EPFL, Switzerland) is used. Recon-

146 structions are performed with the XAct software provided by RX-Solutions (Annecy, France), with

147 appropriate beam-hardening corrections applied. The PEEKcell is fixed on the rotating table, as close

148 as possible to the x-ray source, for a maximal use of the x-ray conical beam. All scans are performed

149 in temperature controlled environment of 21°C.

150   A cylindrical cell made out of PEEK is used for the application of the various boundary conditions,

151 that are explained in detail in the following sections. The so called PEEKcell, is designed to host

152 5 mm × 5 mm cylindrical samples and can sustain a maximal pressure and temperature of 20 MPa

153 and 80°C respectively (Stavropoulou and Laloui, 2022). An entry on each side of the cell (top and

154 bottom) allows the application of confining pressure (top) and pore pressure on the sample (bottom).

155 The cell is disconnected from the pressure controllers and transported under the given pressure state

156 in the tomograph. To monitor the pressure level during the scans, a pressure transducer is placed on

157 each side (see Figure 1).

158   The samples are cut to cylindrical shape of d = h = 5 mm; first sized down in rectangular pieces

159 with a saw and then reduced to the desired size manually using fine sand paper (P240). This technique

160 has been preferred (to a mechanical lathe for example) in order to avoid overheating the sample during

161 preparation. The resaturation of the samples has been achieved progressively under free swelling

162 conditions by exposing the samples in a controlled relative humidity (RH) environment with the use

163 of an appropriate saline solution (Romero, 2001); first to RH = 75% (NaCl) and then RH = 98%

164 (K_2SO_4) until mass stabilisation. Before testing, samples have achieved a close-to-full saturation

165 state, corresponding to a measured water content w_{resat} = 6.1 - 6.8 %, i.e. within the range of full
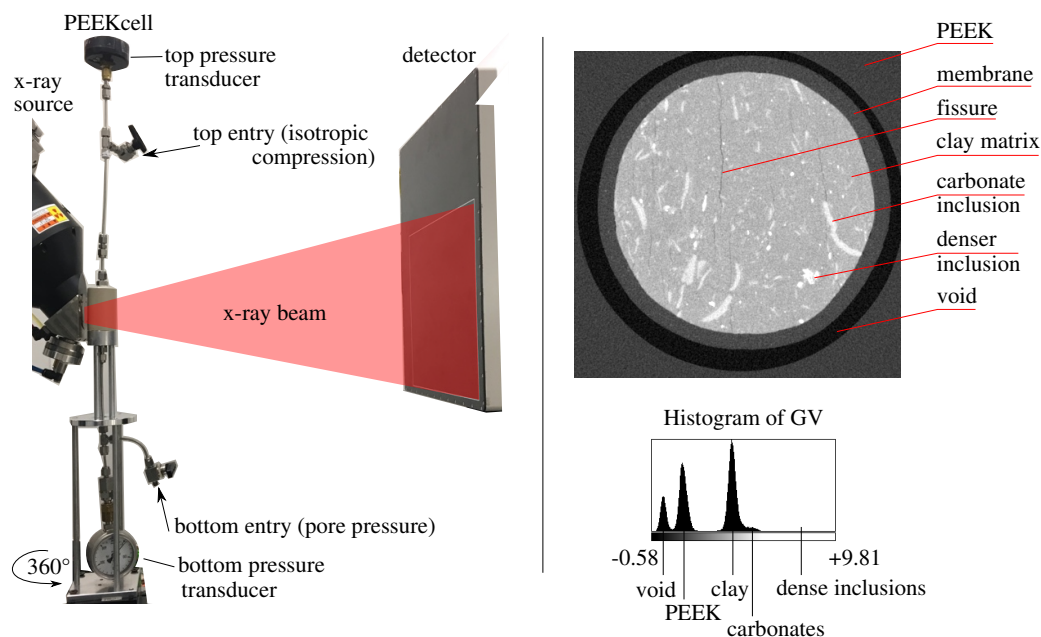
Figure 1: (left:) PEEKcell setup in the x-ray tomograph, (right:) horizontal slice of a reconstructed x-ray image and the corresponding histogram of greyvalues

166 saturation (Bossart and Thury, 2011).

167   In this work, the micro-structural modifications due to long-duration CO_2 exposure are investi-

168 gated with *post-mortem* measurements and analysis, *i.e.* after removing the applied pressures. Then,

169 the occurring kinematics on Opalinus Clay that is exposed in direct contact (no sealing membrane)

170 with supercritical CO_2 is examined with *in-situ* measurements, *i.e.* while under pressure in the cell.

171 According to the volumetric response of the sample and the corresponding GV of the images, the

172 CO_2 uptake is investigated and visualised for the first time.

173   When supercritical CO_2 is injected, a thermal jacket is used around the cell and the applied tem-

174 perature is monitored with a thermal sensor that is placed between the jacket and the PEEKcell. For

175 achieving a maximal resolution and x-rays penetration the thermal jacket is removed during the scans.

176 Inevitably, this leads to CO_2 phase change from supercritical (lower density) to liquid (higher density)

177 and consequently to pressure drop under constant volume conditions, *i.e.* conditions during scanning.

178 In order to minimise this pressure drop, the cell is exposed to the scanner's temperature (21°C) two

179 hours in advance while maintaining the pressure at the desired level (pressure pump connected), in or-

180 der to avoid pressure loss due to phase change during the scan. The possible implications of this CO_2

181 phase transition before the scans on the given testing campaign are discussed in the corresponding

182 section of direct exposure to supercritical CO_2.

183 2.2 Image Analysis

184 The result of an x-ray tomography is a 3D x-ray attenuation map of the scanned sample that is asso-

185 ciated to the 3D density map of the material. For instance dense phases in the material (*e.g.* mineral

186 inclusions) attenuate more x-rays than lower density phases (*e.g.* cracks, pores). The different den-

187 sity (attenuation) levels reflect in the grey level values (GV) of the reconstructed 3D x-ray image;

188 higher GV corresponds to denser phases and lower GV to lower phases as indicated in Figure 1-right.

189 Changes in the GV of a scanned sample in time or due to application of a different load allow the ob-

190 servation and quantification of localised micro-structural modifications (*e.g.* crack opening/closing,

191 swelling/shrinking) which can subsequently be translated to 3D strain fields with Digital Volume Cor-

192 relation (DVC). In this work, the open source SPAM software (Stamati *et al.*, 2020) is used for the

193 DVC analysis.

194 In DVC, two images are required; an initial (reference image) and a deformed one. In the case

195 of local-DVC (that is used for the image analysis in this work), a grid with a given node spacing

196 is defined and at each grid point a centred window is extracted. For each of these subvolumes a

197 linear deformation function Φ is calculated so that $im_{def}(\Phi \cdot x) = im_{ref}(x)$. The function Φ accounts

198 for translation, rotation and stretching and its calculation is optimised by solving an iterative problem

199 that minimises error based on the classic sum of squared difference (SSQD). While DVC can calculate

200 a strain field and that can then be applied it on an image, it does not take into account by definition the

201 variations of the GV due to the corresponding strain. GV correction due to deformation is going to be

202 applied in this work as per (Stavropoulou *et al.*, 2020) where the aim is to investigate phase changes

203 due to chemical reactions between the in-contact CO_2 with the same material.

204 All scans of each type of test are performed under the same conditions and with the same scanning

205 parameters. Nevertheless, noise, artefacts or other external changes may be present between the dif-

206 ferent scans (that in some cases are performed in month intervals). To improve the accuracy of image

207 analysis and minimise the GV variations due to measurement conditions rather than real changes in

208 the material, all images from a testing campaign are normalised based on GV of materials, the density

209 of which is not supposed to vary between the different scans; here PEEK and aluminium. The proce-

210 dure of the GVs normalisation is explained in detail in the Appendix and results in scaling the given

211 images so that the voxels that correspond to void are set to GV = 0 and those of PEEK correspond to

212 GV = 1.

213   Finally, for the strain field calculation, the occasional rigid-body transformation of the sample

214 (translation and rotation) due to transportation and re-installation of the cell in the tomograph, is

215 calculated based on the a single Φ function on the entire image (so called registration) and removed.

216 DVC is then performed between the reference image and the deformed ones from which rigid body

217 motion has been corrected. The displacement field is then calculated and translated to strain assuming

218 small transformations (see all details in Stamati *et al.*, 2020). The above principles and conventions

219 are applied for the analysis of the different series of x-ray scans that are presented in the following.

3   Mineralogical analysis and long-term structural modifications

221 In this section, the long-term chemo-mechanical interactions that can occur between CO_2 and a shaly

222 caprock are explored.   When CO_2 is placed in contact with the pore water of the shaly caprock

223 material, it results in acidification of the pore fluid – by means of diffusion – and therefore resulting

224 in an alteration of the chemical equilibrium. For instance, pre-existing carbonate crystals might be

225 dissolved by the acidic fluid and enhance the material's transport properties (Busch *et al.*, 2008;

226 Espinoza *et al.*, 2011; Jia *et al.*, 2018). On the other hand, incorporation of supercritical CO_2 in

227 micro-structural interlayers can induce the beneficial swelling of smectitic clays (as is expected in

228 self-sealing for nuclear storage applications), but it is not clear whether such a response would occur

229 *in situ* since such tests have taken place under unconfined conditions (batch reactors) (Alemu *et al.*,

230 2011).

231   Taking into account the small size of the samples (5 mm × 5 mm), first a mineralogical analysis

232 of different Opalinus Clay samples is performed with x-ray diffraction (XRD) measurements, in order

233 to evaluate the mineralogical variability. Then the mineralogical map of an Opalinus Clay sample is

234 studied with SEM-EDX (scanning electron microscopy and energy dispersive x-ray) measurements

235 and the identified mineral locations is directly compared and identified in the corresponding slices

²³⁶ from the x-ray tomography image of the same sample. This combined analysis aims to locate and

²³⁷ demonstrate elements in the sample that may favour chemical interactions in the long-term presence

²³⁸ of CO_2 (*e.g.* Ca, C, Si, S, O *etc.*) that is here investigated with x-ray tomography by means of

²³⁹ occurring micro-structural modifications (fissuring, swelling, self-sealing *etc.*).

²⁴⁰ Table 1 shows the mineralogical composition of four sister Opalinus Clay samples from XRD

²⁴¹ measurements. The fit was optimised on one sample and to increase comparability, the next fits were

²⁴² done by keeping all refined parameters and replacing the data file on the current model. Even though

²⁴³ the results are quite approximate, a similar quartz and clay content is measured for all samples except

²⁴⁴ for illite that presents variations up to 8%. In the lower illite-rich samples a higher calcite content is

²⁴⁵ measured with values that vary among the different samples from 13% to 24%. The mineral content

²⁴⁶ of sample A (in bold) is measured after long-term exposure to CO_2. It presents a high clay content

²⁴⁷ that is unclear if it is affected in any way by its previous interaction with CO_2 since its overall mineral

²⁴⁸ content falls within the variability of the other three *untreated* samples. Sample A is used to compare

²⁴⁹ the results from all different analysis tools that are employed for this study.

Opalinus Clay (wt%)	A	X	Y	Z
Calcite	**21**	13	16	24
Quartz	**13**	13	14	11
Chlorite	**15**	15	13	17
Kaolinite	**3**	2	2.5	1.5
Illite	**45.5**	53.5	52	45.5
Siderite	**2**	2	2	11.5
Pyrite	**0.5**	0.5	0.5	0.5

Table 1: Mineralogical composition of four sister Opalinus Clay samples based on x-ray diffraction

²⁵⁰ In order to confirm the mineralogy of the inclusions identified from x-ray tomography, sample A

²⁵¹ has been subjected to a SEM-EDX analysis. The height of the sample is carefully reduced to the height

²⁵² of the horizontal slice of Figure 2-a using again light sandpaper (the traces of which are apparent in

²⁵³ the SEM images). Figure 2 presents the combined information obtained both from x-ray tomography

²⁵⁴ and SEM-EDX at the same horizontal slice. In Figure 2 (a) the x-ray slice, the different GV levels

²⁵⁵ highlight the distribution of the different inclusions in the clay matrix, the mineralogy of which is

²⁵⁶ identified from the EDX analysis. In fact, there are two sets of inclusions as revealed from the GV

²⁵⁷ histrogram plotted in Figure 2 (b). This is more clear when a bilateral filter is applied (red histogram)

₂₅₈ that unveals a second peak that represents the lower GV inclusions.
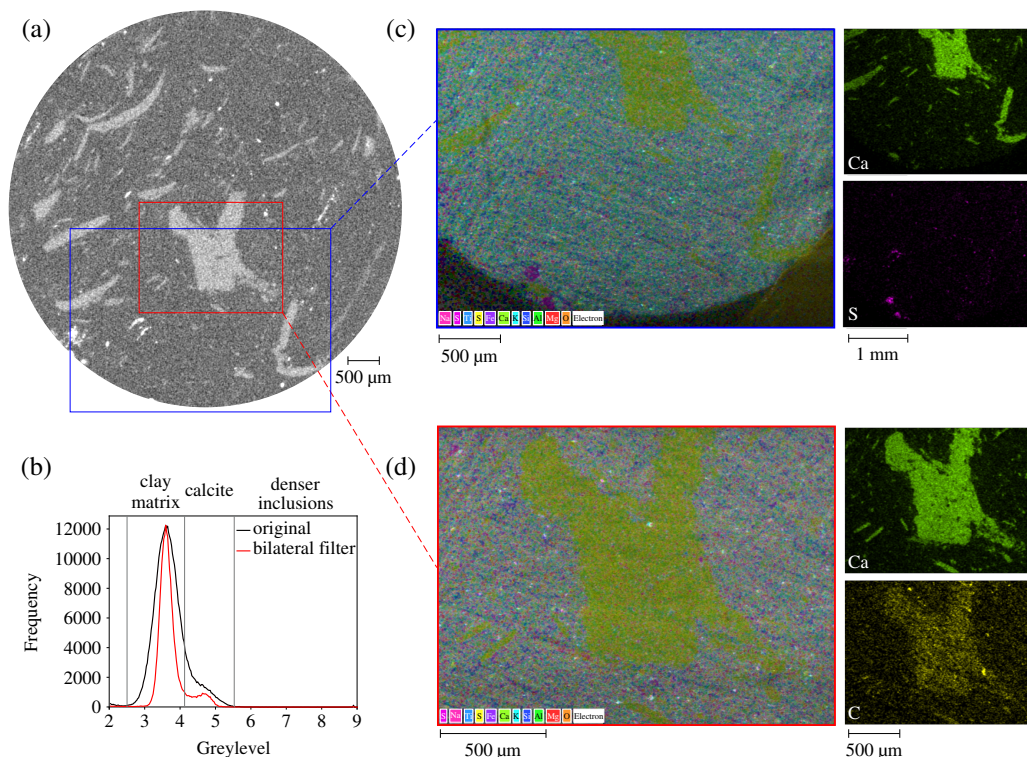
Figure 2: Identification of the inclusions' mineralogy combining x-ray tomography and SEM-EDX – (a) horizontal x-ray tomography slice, (b) histogram of GVs of the top horizontal slice, (c) SEM-EDX map corresponding to the blue window of the x-ray slice highlighting all identified elements and the areas rich in Ca and S, (d) SEM-EDX map corresponding to the red window of the x-ray slice highlighting all identified elements and the areas rich in Ca and C

₂₅₉ These lower GV level inclusions are rich in calcite (Ca) and carbon (C) as revealed from the EDX

₂₆₀ images (Figure 2 (c) and (d)). This type of inclusions are therefore more prone to undergo dissolution

₂₆₁ in the presence of CO_2. The denser inclusions (whiter inclusions in Figure 2 (a) at the bottom left of

₂₆₂ the sample) seem to be rich in sulphur (S) (Figure 2 (c)), a main element of pyrite (FeS_2) the density

₂₆₃ of which is very high. This supplementary EDX measurement reveals that the information from the

₂₆₄ 3D x-ray images is even richer than what has widely been used for now.

₂₆₅ Sample A is the same sample that has been used in (Stavropoulou and Laloui, 2022); it has first

₂₆₆ been scanned in the x-ray tomograph under unconfined conditions, then after application of confine-

₂₆₇ ment (10 MPa) followed by CO_2 injection up to 8 MPa (pixel size 7.8 μm). After CO_2 breakthrough,

268 it has been let under constant volume conditions in the PEEKcell for 9 months and scanned again in

269 the x-ray tomograph after pressure release (same pixel size and scanning parameters). It is important

270 to mention that there has been pressure loss during these 9 months that has not been properly moni-

271 tored. Nevertheless, the results present great interest that is not necessarily impacted by this pressure

272 loss.
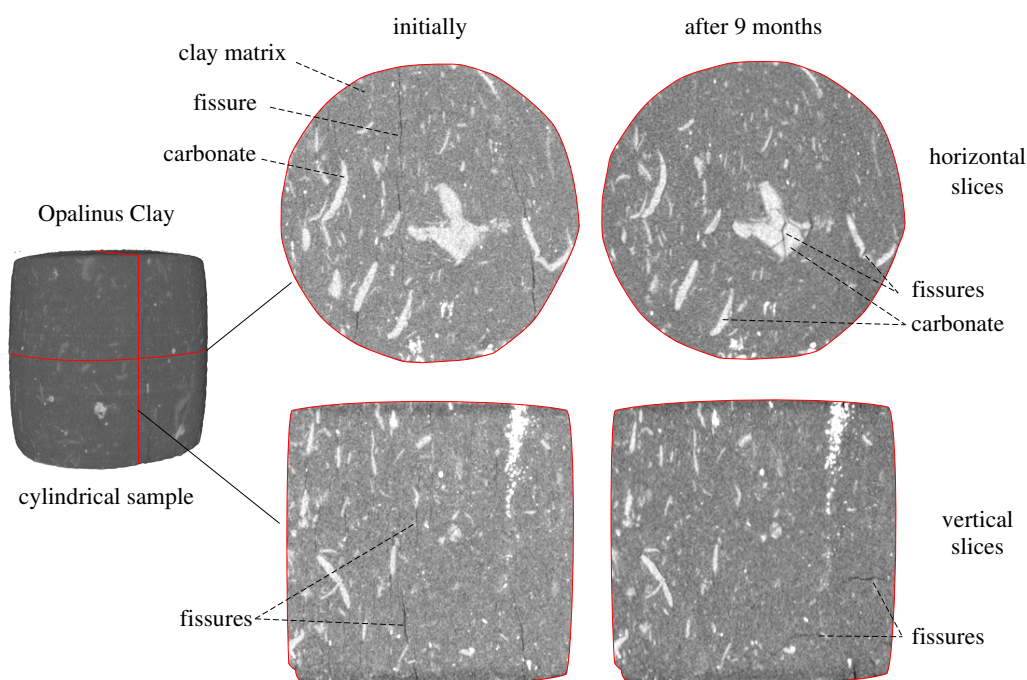
Figure 3: Horizontal and vertical slices of x-ray tomography on the same Opalinus Clay sample with highlighted fissures (in black) under unconfined conditions at its initial state (left) and after 9 months CO_2 exposure (right). The horizontal slices (top) highlight the fissuring of the carbonate phase due to dissolution and the self sealing of the clay matrix pre-existing fissures under long-term confinement; the vertical slices (bottom) highlight the fissure rearrangement and change of orientation that took place in time.

273 Figure 3, shows a horizontal and vertical slice of two x-ray scans of sample A, initially and after

274 9 months of CO_2 exposure, both in unconfined conditions. The micro-fissures have been manually

275 highlighted in black for more clarity, but the entire volumes can be found at their original form in

276 the supplementary material. The initial image of the sample reveals a vertical bedding orientation

277 according to the orientation of the pre-existing fissures in the clay matrix. After 9 months of CO_2

278 exposure there are two important observations to be pointed out. First, clear fissures in the carbonate

279   phases have been formed revealing the calcite dissolution for the first time from x-ray images and

280   under non-extreme (if not realistic) testing conditions. In addition to the fissuring of the carbonate

281   inclusions, a disappearance of the initially pre-existing fissures in the clay matrix is observed. This can

282   be explained first by means of self-sealing behaviour of the material under long-duration application

283   of confinement and then by precipitation of Si-reach zones that are not distinguishable from the x-ray

284   images, since they have similar density with the clay minerals. Indeed, (Prakash *et al.*, 2022) pointed

285   out a more pronounced precipitation activity in zones parallel to the direction of the bedding plane.

286   For a better understanding of the micro-structural modification of the sample after long-term CO_2

287   exposure, the orientation of the minimum eigenvectors (longest axis) of the inclusions and micro-

288   fissures have been plotted in 3D together with their projection in the 2D plane, as shown in Figure 4.

289   Both types of orientation plots are presented for a better demonstration of the result of each studied

290   phase – the 3D histogram is more comprehensible for the cracks' orientation and the 2D projection for

291   the inclusions. For this analysis, a bilateral filter has been applied on the two images to reduce noise

292   and to smoothen the edges between the different phases (clay/cracks, clay/inclusions). In this way a

293   better segmentation of the phases of interest (cracks and inclusions) can be achieved. It is known that

294   segmentation of shale images remains a difficult task due to the heterogeneity and the contrast of the

295   different phase interfaces. Even though these results could be optimised from a quantitative point of

296   view, the overall shape modification of the two segmented phases is realistic.

297   The 2D projection of the min. eigevectors of the inclusions reveals a preferential orientation

298   along the vertical axis – axis parallel to the bedding plane – both initially and after 9 months exposure

299   (Figure 4). The vertical axis of the 2D plots is parallel to the Y axis of the spherical histograms that are

300   plotted in this view to demonstrate the vectors' orientation on the ZY plane. After 9 months exposure

301   to CO_2 the population of inclusions is increased as demonstrated by both plots on the right of Figure 4.

302   This increase in the number of inclusions is a clear indication of carbonate dissolution that resulted in

303   inclusion fissuring and consequently identification of more numerous inclusion *particles*. The main

304   orientation axis after dissolution remains vertical, suggesting that fissuring due to dissolution has

305   mainly occurred along the shortest axis of the inclusions and therefore perpendicularly to the bedding

306   plane.

307   In a similar way, the spherical histograms of the minimum eigenvector of the sample's identified
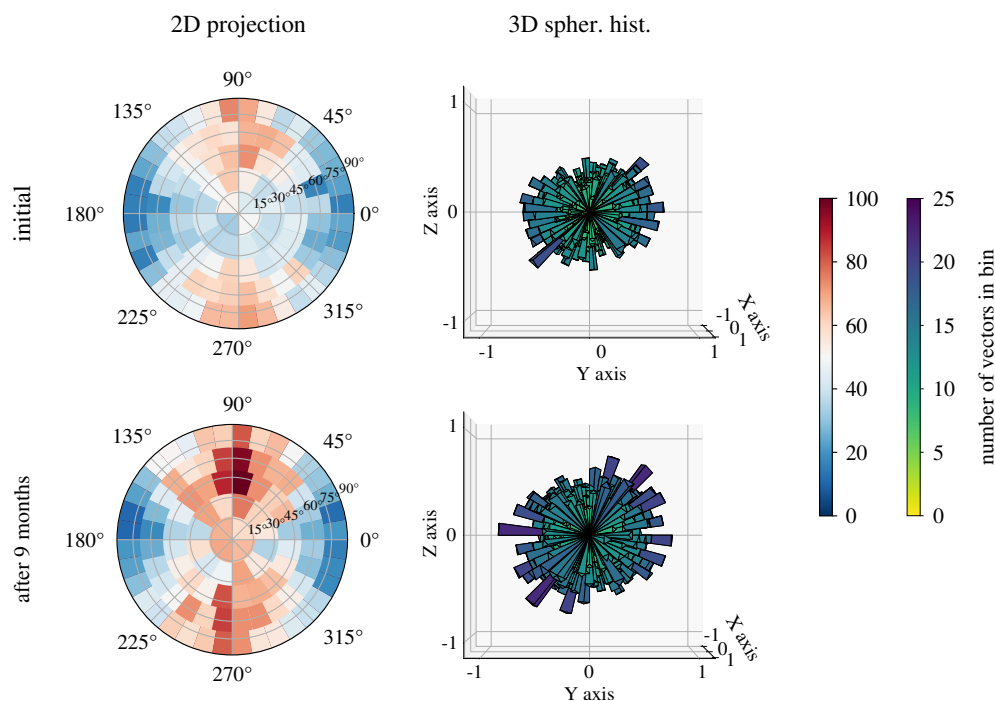
Figure 4: 2D projection (left) and spherical histogram (right) of the minimum eigenvectors of sample's 02 inclusions, initially and after 9 months exposure to CO_2

308 cracks and their 2D projection are plotted in Figure 5; initially and after 9 months of CO_2 exposure.

309 The shape of the 3D histogram initially reveals the sample's anisotropy with a preferential orientation

310 parallel to the bedding plane. This is confirmed by the high number of vectors projected on the vertical

311 axis of the 2D plot – even though the low number of cracks make it harder to evaluate. Interestingly,

312 the shape of the cracks' 3D histogram on the right is very different, confirming the observations

313 and assumptions discussed from Figure 3. First, the number of cracks is reduced, validating the

314 self-sealing (or precipitation) response of the sample after long-duration confinement. Then, most

315 importantly, the orientation of the main cracks has been totally modified and is no more parallel

316 to the bedding. It is not clear whether these new fissures are the result of alteration of the pore

317 fluid's pH that enhances further chemical reactions between minerals that are not detectable from

318 x-rays and CO_2, or whether they are related to mechanical impact from CO_2 breakthrough (see 3D

319 volumetric response after breakthrough in Stavropoulou and Laloui, 2022). In either case, this result

320 points out a potential rearrangement of the fissure network after long-term CO_2 exposure that has not
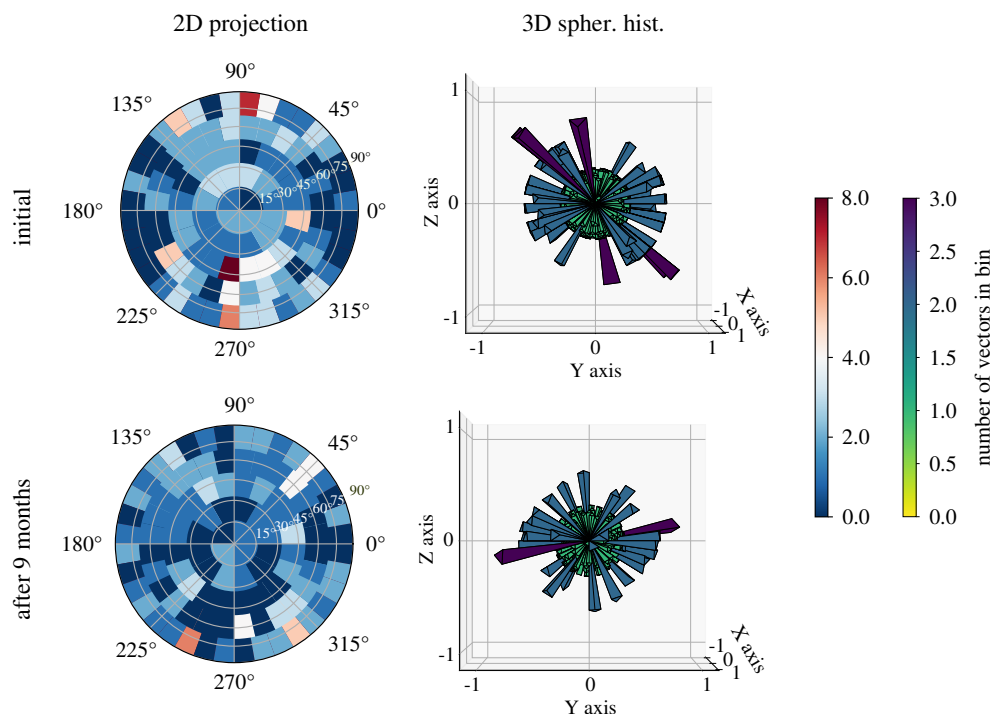
Figure 5: Spherical histogram of the minimum eigenvector of the inclusions and the cracks in sample A, initially and after 9 months exposure to CO_2 (colour represents the number of projected points per bin divided by the median number of points in all bins)

been previously discussed. Most importantly, these results show how little we still know regarding

the coupled long-term THMC response of the caprock/CO_2 interaction at the micro-scale and their

implications to the large scale response. Longer-duration testing under realistic boundary conditions

are required for a better understanding of the complex mechanisms that occur.

Finally, in the aim of a better visualisation of the texture of the carbonic inclusions, the SEM

image of the same (unpolished) slice with Figure 2 is presented in Figure 6. For the SEM images,

two detectors have been used; (top) a secondary elements detector that basically illustrates the sur-

face topography; and (bottom) a backscattered electrons detector that shows a Z contrast, *i.e.* lighter

elements (such as Si, Al, O, K) are darker and heavier elements (here Ca or C) are brighter. The

secondary elements detector does not reveal any information regarding the targeted inclusion other

than the fewer sandpaper traces that are very obvious on the softer clay matrix. On the other hand,

the backscattered electrons detector provides a better distinction between the two phases. The higher
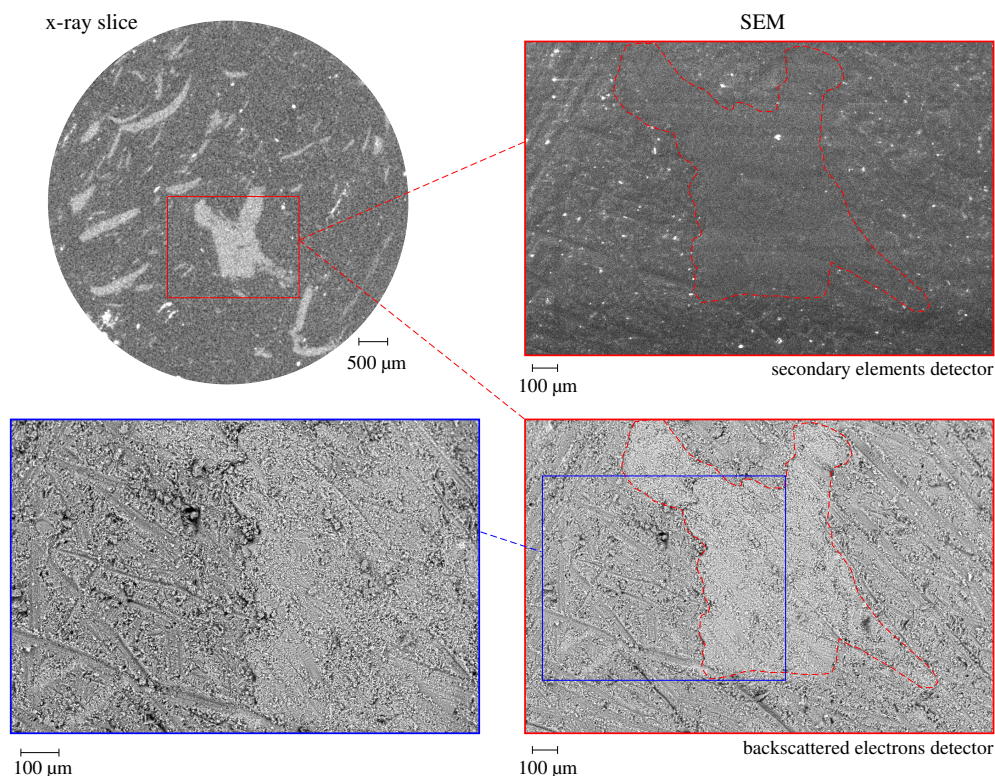
Figure 6: Opalinus Clay core sample

resolution of SEM allows a better visualisation and understanding of the interface between the carbonate inclusion and the clay matrix that is otherwise not visible with x-rays. While the resolution is still in the micrometric scale and no nanometric pores can be detected in either types of images, a distinct calcite/clay interface of increased porosity is revealed in the zoomed area of the bottom SEM image (blue window). Indeed, this is a good confirmation of what is reported in (Minardi *et al.*, 2021) carbonate-rich Opalinus Clay; the pore size distribution is bimodal with a second dominant pore size between 50-100 μm corresponding to the interface of carbonate/clay particles. This high inter-particle porosity can serve as a preferential CO_2 pathway and eventually enhance geochemical interactions; in this case carbonate dissolution.

4 Direct exposure to supercritical CO_2

In this part, the interaction of an Opalinus Clay sample with supercritical CO_2 is evaluated in time by means of quantitative 3D x-ray image analysis. The unjacketed caprock sample is exposed from all sides (equilaterally) to direct contact with supercritical CO_2 (p = 10 MPa and T = 34°C) and regular x-ray scans (resolution 5.38 μ/m) are performed for the study of its volumetric and micro-structural response. The water saturated sample is mounted in the PEEKcell and a first scan (00) is performed under initial ambient unconfined conditions. Then, the target pressure and temperature are applied and the sample is let to interact with the in-contact CO_2. Further scans of the sample are performed while under pressure in the PEEKcell after 13 days (scan 01), 30 days (scan 02) and 56 days (scan 03), as well as after release of pressure and temperature (scan 04).

4.1 Volumetric response

The 3D volumetric response of the caprock material under the above mentioned conditions are evaluated and quantified by means of DVC analysis. As explained earlier, to properly compare and analyse the acquired images, the occasional rigid-body transformation (translation and rotation) is removed so that the images are well aligned as shown in the left column of Figure 7. The middle vertical slice of the tested sample reveals the pre-existence of 3 principal fissures parallel to each other and parallel to the bedding orientation of the sample, *i.e.* perpendicular to the vertical axis of the sample. These micro-fissures of initial max. aperture $\approx$ 30 μm may have been induced during sample preparation and/or during resaturation under free swelling conditions. Their existence is not necessarily an issue for the given study; on the contrary they can provide important insight into the impact of their presence upon interaction with CO_2. Looking more closely at the microstructure of the middle slice in Figure 7 an increase of the bottom principal pre-existing fissure can be observed, as well as the creation and propagation of additional new micro-fissures at the bottom of the sample; between the bottom left inclusion structure and the lower principal fissure.

For a more quantitative analysis of the localised response of the sample, the volumetric strain is calculated in 3D between each scan and the initial state of the sample (scan 00) that is used as reference. For the DVC analysis, the chosen parameters (half window size, node spacing *etc.*) are detailed with the additional provided data online. The map of the calculated volumetric strain of each
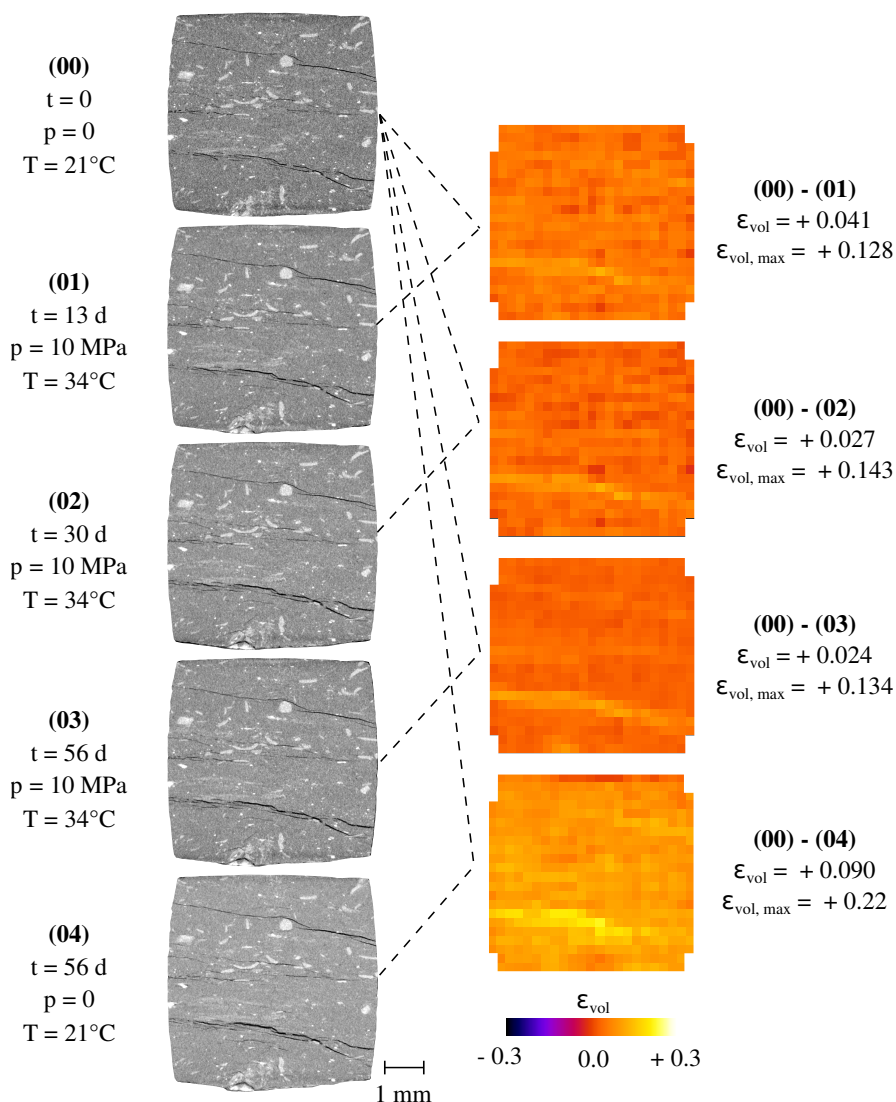
Figure 7: Volumetric response of the middle vertical slice of the Opalinus Clay sample in time after exposure to supercritical CO_2

370 scan presented on the right column of Figure 7 where the corresponding middle vertical slice is shown

371 – it must be noted that the values of measured volumetric strain, total (ε_{vol}) and maximum ($\varepsilon_{vol,max}$)

372 correspond to the entire 3D volume. In all scans a more pronounced expansion is measured on the

373 location of the lowest pre-existing micro-fissure ($\varepsilon_{vol,max}$). Only after 2 months of CO_2 exposure (scan

374 03) a slight expansive activity may be measured around the othe two pre-existing ones. The overall

375 expansive response of the sample (positive ε_{vol}) is clearly dominated by the expansion of the fissures

376 that remains mostly constant in time For the rest of the material it is hard to observe a clear pattern,

377 nevertheless the calculated volumetric strain reveals an initial expansion ($\varepsilon_{\text{vol}_{00\text{-}01}} = + 0.041$) that in

378 time reduces ($\varepsilon_{\text{vol}_{00\text{-}02}} = + 0.027$) and stabilises ($\varepsilon_{\text{vol}_{00\text{-}03}} = + 0.024$). Finally, upon pressure decrease,

379 the material expands in a pronounced way ($\varepsilon_{\text{vol}_{00\text{-}03}} = + 0.090$) not only at the lower crack zone but

380 everywhere in the sample due to stress relaxation, as explained in the following.

381   The interpretation of this response is not straightforward since the sample is subjected to complex

382 THMC boundary conditions. In theory, the application of constant pressure equilaterally and directly

383 in contact with a fully water saturated sample is not supposed to affect the applied effective stress

384 that should remain zero. In other words, since CO_2 is *injected* equilaterally in the unjacketed sample,

385 the concept of effective stress is not valid, neither is the concept of hydraulic fracturing with the

386 increase of pore pressure as it is the same with the applied skeleton pressure. However, the presence

387 of pre-existent fissures suggests that the sample cannot be realistically fully saturated and there matric

388 suction must be present locally in the fissured and partially saturated zones. Upon high pressure CO_2

389 exposure suction breakdown occurs locally (decrease of effective stress) and the sample swells until

390 stabilisation at full saturation – water + CO_2. This interpretation can confirm the initial volumetric

391 activity that eventual stabilises in time.

392   Local modification of the effective stress is not the only mechanism that may take place upon

393 exposure of a shale sample to supercritical CO_2. Temperature increase (34°C) induces thermal ex-

394 pansion to the sample that can indeed justify the rather isotropic expansion measured in scan 01.

395 Another important aspect that has been little discussed in the literature is the dessication of the ma-

396 terial when in contact with CO_2. Indeed, the pore water of the material evaporates in the anhydrous

397 CO_2 resulting desaturation which can result to further crack opening (expansion) and pore collapse

398 in the clay matrix. This dessication effect could explain the lower volumetric expansion in time until

399 eventual equilibrium. This little discussed interaction can occur in real field conditions at the bot-

400 tom of the caprock formation in contact with the buoyant CO_2, leading to partial desaturation of the

401 caprock and threaten its mechanical integrity and sealing capacity.

402   To better understand the impact of the afore mentioned coupled THM mechanisms, the evolution

403 of the fissures' volume in the different scans is presented in Figure 8. For their calculation the same
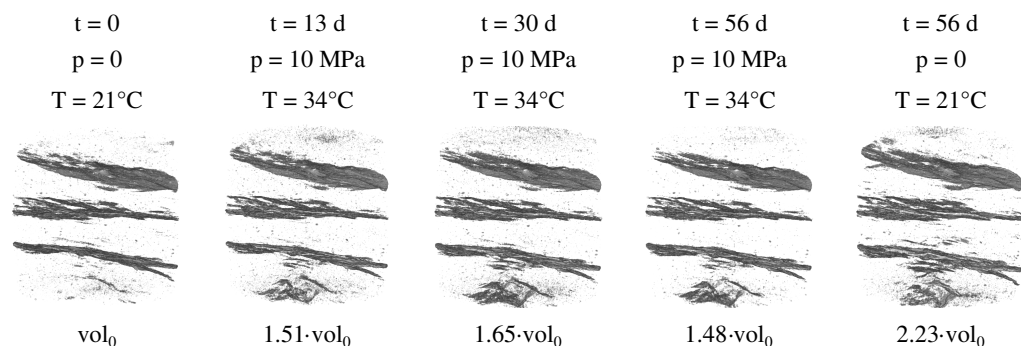
Figure 8: Evolution of pre-existing fissures and appearance of new ones after direct exposure to supercritical CO_2 (illustration in 3D)

GV threshold has been used for all the normalised scans. Once again, segmentation of shale images is a difficult exercise, the optimisation of which is out of the scope of this study. The obtained results are considered sufficient to demonstrate the overall behaviour of the material. While the volumetric increase of the pre-existing fissures has already been identified from the calculated volumetric maps of the entire sample, Figure 8 clearly demonstrates the creation and propagation of a new family of fissures at the bottom of the sample. These new fissures demonstrate in a very clear way the dessication effect of anhydrous CO_2 explained above. Additional chemo-mechanical mechanisms may contribute to the initiation of these micro-fissures that are impressively localised in a calcite-rich area at the bottom of the sample (see x-ray images in Figure 7). Eventual dissolution aspects are hard to interpret since preferential fissuring patterns in calcite-rich zones may primarily be due to increased porosity between the calcite and the clay mineral interface (as shown in Figure 6).

4.2 CO_2 uptake

After the in-depth analysis of the microstructural response of the caprock material during direct contact with supercritical CO_2, an attempt to visualise and quantify the CO_2 penetration in the material is attempted in this part of the study. The analysis is based on the evolution of the x-ray images' GVs after correction due to volumetric strain as per (Stavropoulou *et al.*, 2020). This approach is quite ambitious in the context of CO_2 uptake, since the density variations due to supercritical CO_2 invasion are very slight. This is why normalisation of the images' GVs is imperative for this kind of analysis (see Appendix).

Taking into account the measured strain field from the DVC analysis, the variation of the x-ray attenuation coefficient (μ_x) in time is corrected and measured. Volumetric strain results in density variation (and therefore μ_x variation) ~~that~~ is manifested in the GVs level of the deformed image via a linear relationship. A simple example to better understand this reasoning is the case of thermal expansion with no mass transfer, where the density of the material is expected to reduce, and consequently the attenuation field μ_x or GVs to decrease proportionally to the change in density. Any additional GV variation is therefore assumed to be due to additional mass transfer (gain or loss); in this work due to CO_2 uptake. According to (Stavropoulou *et al.*, 2020), the attenuation variation of a sample is calculated as a function of the mechanical volumetric strain assuming mass conservation:

$$\Delta\mu = -\varepsilon_v \cdot \mu_0 \tag{1}$$

where ε_v is the measured volumetric strain of the sample and μ_0 is the initial attenuation of the image (before loading).

In order to measure the additional changes of GVs due to mass transfer, the calculated strain field is applied on the reference image (scan 00), while taking into account the corresponding GV correction. Then, simple subtraction of the deformed image (with corrected GVs due to volumetric variation) from the corresponding original image (*e.g.* 01 minus 00_def_to_01) results in the uptake or loss of mass. The result of this analysis is presented in Figure 9, where the chosen colourbar represents density (in terms of GV) increase (red) or decrease (blue).

The maps of the GV variation show a density decrease overall during the first month of exposure (00-01 and 00-02). This response can be supported by the sample's desaturation discussed earlier; in fact, invasion of anhydrous CO_2 in the material partially occurs through water evaporation, therefore the material is filled up with a fluid of lower density. While these results are somewhat noisy for precise conclusions, nevertheless a more pronounced *density decrease* is obtained during the first month at the lower part of the sample where *crack initiation* occurs. On the other hand, around the zones of the *pre-existing fissures* a *density increase* is measured; in this case the non saturated zones around these fissures might have been filled in with CO_2. It has to be noted that this approach is even less accurate around ~~in the~~ crack locations. This is because the obtained fields are the result of the subtraction between the initial least fissured image (00) with a future deformed image (*e.g.* 02) that has more fissures – the application of the calculated deformation field on 00 cannot create these new
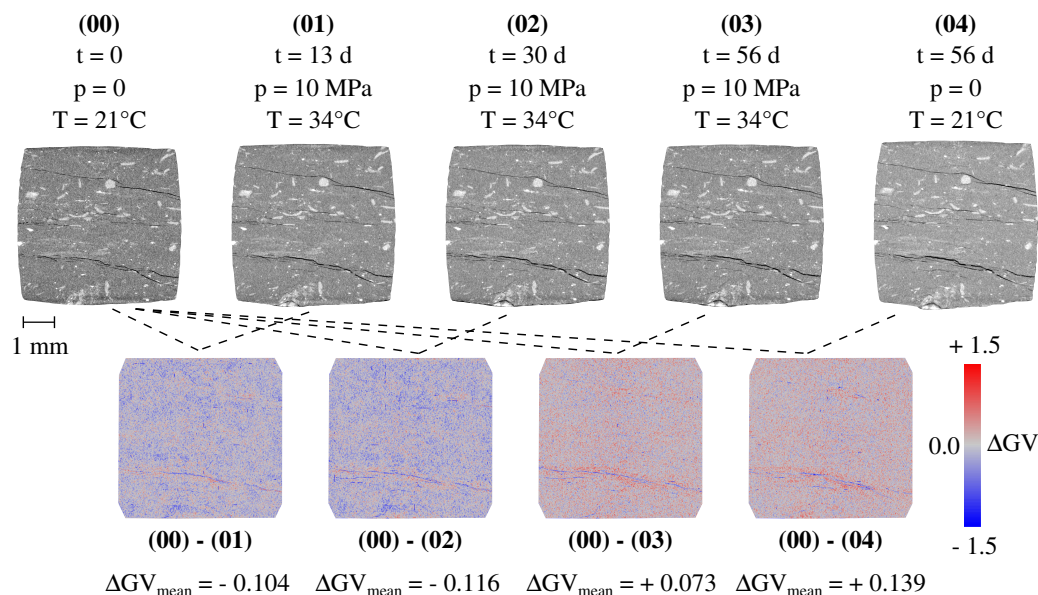
Figure 9: Fields of the grey value changes of the caprock material in time after removing the changes ~~due~~ volumetric strain

fissures this is why directly on the fissures the density will be always decreasing (blue).

Two months after CO_2 exposure, the overall density of the material eventually increases in a relatively homogeneous way, if not with more noticeably around the lower pre-existing fissure. It is interesting to notice that between scans 02 and 03 the volumetric activity that was measured is almost negligible. This density increase under constant volume reveals the saturation of the material with CO_2. Indeed, unlike the previous two fields, here the material seems to be in equilibrium indicating that CO_2 has invaded it in its entity. Final CO_2 pressure release (00-04) leaves the sample with an overall increased density, in particular at the zones around the fissures and at the bottom. This final result may indicate chemo-mechanical or CO_2 trapping phenomena that may occurred during the two month exposure. This is a first attempt to visualise CO_2 invasion in a caprock material and even though it is quantitative in terms of GV levels, their physical interpretation in terms of *e.g.* actual CO_2 volume increase or water decrease requires further studies and measurement for the calibration of the different phases' GVs.

5 Discussion and Conclusions

In this work the interaction between the Opalinus Clay, a caprock representative material, with CO_2 is studied with x-ray tomography imaging. The different results and observations reveal the complex response of this material due to multiple coupled phenomena that occur in parallel. Exposure to supercritical CO_2 implies temperature increase of the material that results in thermal expansion (TM coupling). This expansion leads to inevitable desaturation of the material (TH coupling). At the same time, the live observation of the caprock material in time revealed another important aspect when anhydrous CO_2 is in contact with the water saturated sample; the pore water evaporates in the anhydrous CO_2 causing further dessication of the material that starts fissuring. Fissures, whether pre-existing in the material or new ones, play an important role on the CO_2/caprock interaction. They drive most of the volumetric and hydraulic phenomena; swelling, desaturation, uptake, breakthrough. Their impact is still not well understood, in particular under realistic field conditions.

The long-term impact of CO_2 on the micro-structure of the shaly material is for the first time visualised with x-ray tomography on a solid sample and under non-extreme temperature and pressure conditions. Calcite dissolution is identified in carbonate-rich zones that after 9 months of exposure they were fissured (CM coupling). The mineralogical composition of these denser (white) inclusions in the x-ray images has been confirmed from SEM-EDX measurements. Segmentation and labelling the inclusions before and after long-duration CO_2 exposure confirmed an increased number of inclusions due to breakage (dissolution) the mean orientation of which did not significantly evolve. A similar analysis has been made on the fissure network in the clay matrix of the sample before and after long-term exposure. The principal crack orientation in the sample is initially parallel to the bedding orientation of the shaly material. These fissures close with the application of confinement as shown in (Stavropoulou and Laloui, 2022) but very interestingly they do not re-appear 9 months later after pressure release. This result demonstrates the self-sealing response of Opalinus Clay (HM coupling). In addition to the closure of pre-existing fissures, the 9 months x-ray scan revealed the appearance of some new micro-fissures in the clay matrix (other than the fissures in the calcite zones) surprisingly in a perpendicular direction to the bedding. This aspect of potential re-arrangement of the fissure network of the material is demonstrated for the first time and could be due to additional chemo-mechanical mechanisms within the clay matrix or related to CO_2 breakthrough that due to

493 self-sealing of the initial micro-fissures initiated a new optimal pathway throughout the sample.

494   Finally, the CO_2 uptake in the caprock material has been investigated by combining the calculated

495 strain fields and the GV variation of the acquired x-ray images. CO_2 penetration in the sample has

496 been identified two months after initial exposure. It is hard to interpret the multi-phase fluid interac-

497 tion in the porous space of the material prior to two months due to the multiple THMC phenomena

498 that take place simultaneously and often counteract each other. It is interesting to note that after

499 CO_2 release the density of the sample remained increased compared to the initial two months earlier,

500 revealing potential CO_2 trapping in the material.
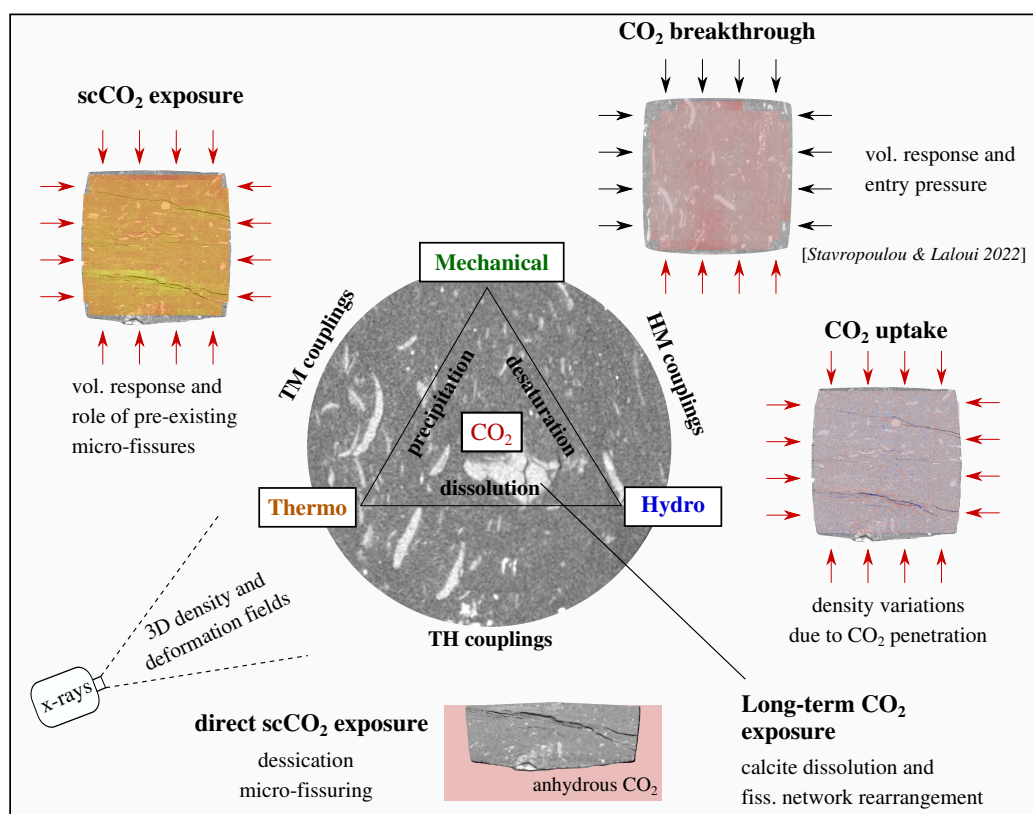
Figure 10: Coupled THMC mechanisms studied with *in-situ* x-ray imaging on small size shale samples

501   Figure 10 sums up the different coupled mechanisms that have been identified in this work to

502 occur during the CO_2/caprock interaction. These topics require undoubtedly further investigation

503 with long-term experiments under continuously monitored conditions. Analysis of the response using

a non destructive tool, *i.e.* x-ray tomography allows the study of the material while under realistic conditions. The study of small shale samples has significantly contributed to the better understanding of the various coupled phenomena, first by achieving better time resolutions under non extreme temperature and pressure conditions, and then by studying the material's response under high spatial resolutions in 3D that revealed mechanisms previously undetectable with conventional testing methods and resolutions.

6 Data availability

The 3D x-ray images that have been used in this paper are provided online in Zenodo [link TBC]. Additional data or results can be provided by the Authors upon reasonable request.

7 Acknowledgements

This study has taken place in the frame of the Spark SNSF CRSK-2_196559 project. The Authors wish to thank the PIXE platform (EPFL) for the assistance during the x-ray tomography scans, as well as the Mont Terri laboratory and SwissTopo for providing the tested Opalinus Clay material.

Appendix A: Normalisation of x-ray tomographies

For the analysis of the attenuation evolution of the images, the different scans are normalised using always as reference scan 00. The objective of this normalisation is to set to zero the voxels that correspond to void in order to be able to more reliably detect density variations. The normalisation is performed considering the parts of the image that are not supposed to vary in density with time; PEEk and Aluminium. Since the void attenuation is changing with the introduction of CO_2, the ratio of the greyvalues (GV) between Aluminium, PEEK and air is considered constant as shown in Figure A1.
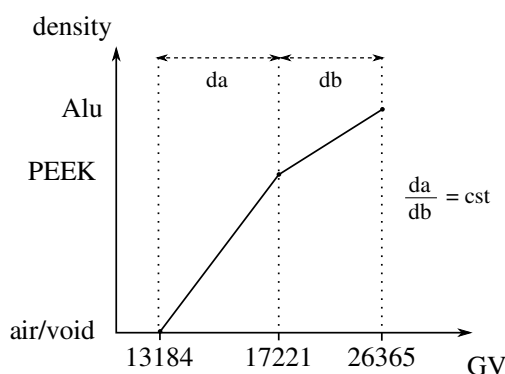
Figure A1: Measured greyvalues as a function of corresponding density in scan 00

GV (32b)	Void	PEEK	Aluminium	da	db	da/db
00	13184 (832)	17221 (833)	26365 (900)	4037	9144	0.44149
01	**13113**	17195 (841)	26442 (910)	**4082**	9247	0.44149
02	**13191**	17237 (839)	26403 (907)	**4046**	9166	0.44149
03	**13450**	17330 (613)	26119 (693)	**3880**	8789	0.44149
04	**13445**	17287 (602)	25990 (699)	**3842**	8703	0.44149

Table A1: Measured (normal font) and calculated (bold font) mean greyvalues (and standard deviation/error in the parenthesis) of the parts of the scan that are not expected to vary in density with time for the normalisation of the images

This ratio is calculated from the reference scan 00 (first row of Table A1) and considered constant

525 in order to deduce the air greyvalue of the rest of the scans. The computed GV of air (first column of

526 Table A1) is then subtracted from each scan, which is then divided by the corresponding PEEK value

527 so that PEEK average value is 1 for the sake of simplicity. The histogram of scan 00 after normali-

528 sation is shown in Figure A2-a, while the histogram after CO_2 introduction (scan 003) is changed to

529 that in Figure A2-b. The GV normalisation of the different scans can improve the volumetric analysis

530 (DVC) and it is indispensa1ble for the detection of density variations.
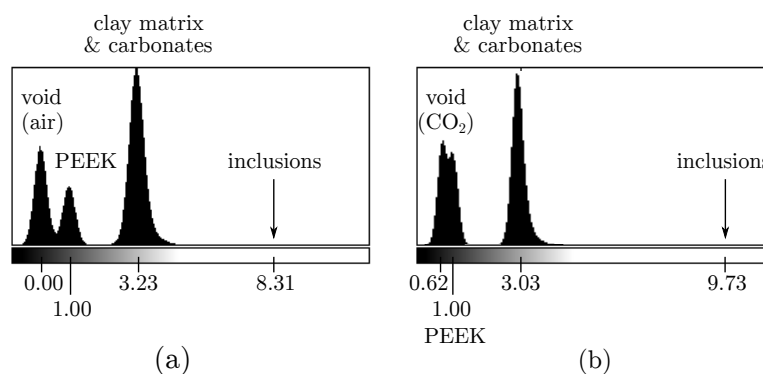
A2: Greyvalues histogram of normalised (a) scan 00 (no CO_2) and (b) scan 01 (with CO_2)

531 Appendix B: Segmentation of the x-ray images

532 The different steps for the segmentation for the different types of phases are illustrated in Figure B1.

533 First, a bilateral filter is applied on the original image in order to smoothen the zones of similar phases

534 and sharpen the edges between different phases (Figure B1-a).

535   The distributions of the GV levels before and after the application of this filter are plotted in

536 Figure B2; a more narrow distribution is obtained after the bilateral filter, providing more precision for

537 the selection of each GV range for the segmentation of the different phases. The resulted segmented

538 slices of the inclusions and the micro-fissures after the application of a threshold GV range are shown

539 in Figure B1-b and c, respectively. In the case of the inclusions, a double cycle of dilation and erosion

540 of the binary image has been applied in order to reduce noise. This is not possible for a further

541 reduction of the noise of the fissures' segmented image due to their 1 pixel thickness.
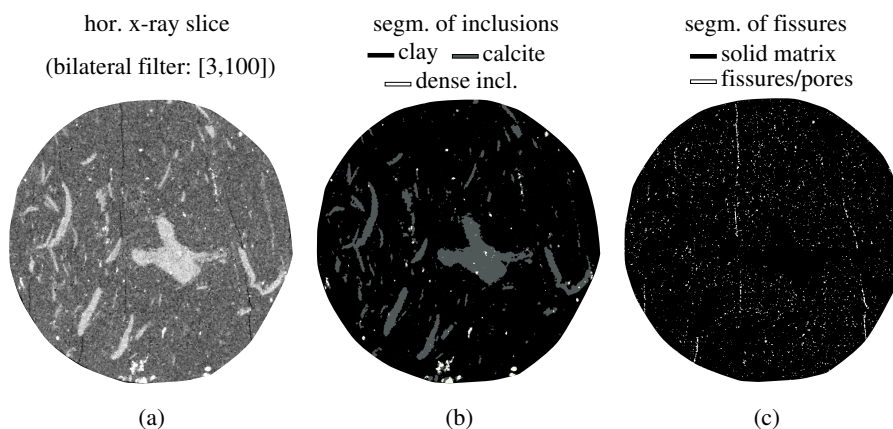
Figure B1: Horizontal slices after the (a) application of a bilateral filter, (b) segmentation of the two types of inclusions (calcite and denser inclusions), (c) micro-fissures
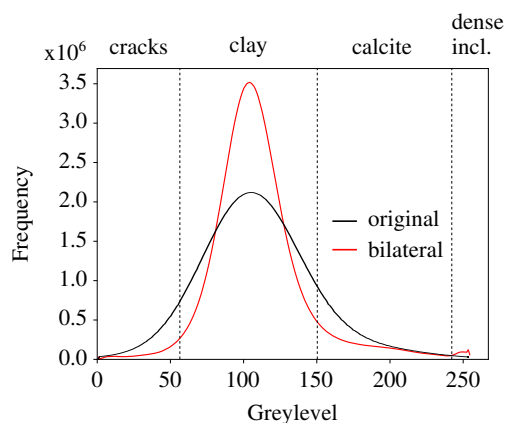
B2: Greyvalues histogram of the original horizontal x-ray slice and after the application of bilateral filter of Figure B2 (a)

References

[1] Alemu, B. L., Aagaard, P., Munz, I. A., & Skurtveit, E.: Caprock interaction with CO2: A laboratory study of reactivity of shale with supercritical CO2 and brine. Applied Geochemistry, 26(12), 1975-1989, https://doi.org/10.1016/j.apgeochem.2011.06.028, 2011.

[2] Amann-Hildenbrand, A., Bertier, P., Busch, A., & Krooss, B. M.: Experimental investigation of the sealing capacity of generic clay-rich caprocks. International Journal of Greenhouse Gas Control, 19, 620-641, https://doi.org/10.1016/j.ijggc.2013.01.040, 2013

[3] Armitage, P. J., Worden, R. H., Faulkner, D. R., Aplin, A. C., Butcher, A. R., & Iliffe, J.: Diagenetic and sedimentary controls on porosity in Lower Carboniferous fine-grained lithologies, Krechba field, Algeria: A petrological study of a caprock to a carbon capture site. Marine and Petroleum Geology, 27(7), 1395-1410, `https://doi.org/10.1016/j.marpetgeo.2010.03.018`, 2010.

[4] Armitage, P.J., Faulkner, D.R., & Worden, R.H.: Caprock corrosion. Nat. Geosci., 6, 79–80, 2013.

[5] Bedford, J., Fusseis, F., Leclère, H. Wheeler, J., & Faulkner, D.: A 4D view on the evolution of metamorphic dehydration reactions. Scientific Reports, 7(1), 1-7. `https://doi.org/10.1038/s41598-017-07160-5`, 2017.

[6] Birmpilis, G., Hall, S. A., Lages, S., & Dijkstra, J.: Monitoring of the nano-structure response of natural clay under mechanical perturbation using small angle X-ray scattering and digital image correlation. Acta Geotechnica, 14(6), 1965-1975, `https://doi.org/10.1007/s11440-019-00832-8`, 2019.

[7] Birmpilis, G., & Dijkstra, J.: Testing sensitive clays through time and length scales. IOP Conference Series: Earth and Environmental Science, 710, 012021, `https://doi.org/10.1088/1755-1315/710/1/012021`, 2021.

[8] Birmpilis, G., Andò, E., Stamati, O., Hall, S. A., Gerolymatou, E., & Dijkstra, J.: Experimental quantification of 3D deformations in sensitive clay during stress-probing, Géotechnique, 1-12, `https://doi.org/10.1680/jgeot.21.00114`, 2022.

[9] Bossart, P. & Thury, M.: Characteristics of the Opalinus clay at Mont Terri, Reports of the Swiss Geological Survey 3, 2011.

[10] Busch, A., Alles, S., Gensterblum, Y., Prinz, D., Dewhurst, D. N., Raven, M. D., Stanjek, H., & Krooss, B. M.: Carbon dioxide storage potential of shales, International journal of greenhouse gas control, 2(3), 297-308, `https://doi.org/10.1016/j.ijggc.2008.03.003`, 2008.

[11] Crisci, E., Ferrari, A., Giger, S. B., & Laloui, L.: Hydro-mechanical behaviour of shallow Opalinus Clay shale, Engineering Geology, 251, 214-227, `https://doi.org/10.1016/j.enggeo.2019.01.016`, 2019.

[12] Delage, P., & Tessier, D.: Macroscopic effects of nano and microscopic phenomena in clayey soils and clay rocks, Geomechanics for Energy and the Environment, 27, 100177, `https://doi.org/10.1016/j.gete.2019.100177`, 2021.

[13] Delage, P., & Belmokhtar, M.: Drained triaxial testing of shales: insight from the Opalinus Clay, Acta Geotechnica, 17(7), 2855-2874, 2022.

[14] Desbois, G., Höhne, N., Urai, J. L., Bésuelle, P., & Viggiani, G.: Deformation in cemented mudrock (Callovo-Oxfordian Clay) by microcracking, granular flow and phyllosilicate plasticity: insights from triaxial deformation, broad ion beam polishing and scanning electron microscopy, Solid Earth, 8(2), 291, `https://doi.org/10.5194/se-8-291-2017`, 2017.

[15] Elkady, Y., & Kovscek, A. R.: Multiscale study of CO2 impact on fluid transport and carbonate dissolution in Utica and Eagle Ford shale, Journal of Petroleum Science and Engineering, 195, 107867, `https://doi.org/10.1016/j.petrol.2020.107867`, 2020.

[16] Espinoza, D. N., Kim, S. H., & Santamarina, J. C.: CO2 geological storage - Geotechnical implications, KSCE Journal of Civil Engineering, 15(4), 707-719, `https://doi.org/10.1007/s12205-011-0011-9`, 2011.

[17] Favero, V., Ferrari, A., & Laloui, L.: On the hydro-mechanical behaviour of remoulded and natural Opalinus Clay shale, Engineering Geology, 208, 128-135, `https://doi.org/10.1016/j.enggeo.2016.04.030`, 2016.

[18] Favero, V., Ferrari, A., & Laloui, L.: Thermo-mechanical volume change behaviour of Opalinus Clay, International Journal of Rock Mechanics and Mining Sciences, 90, 15-25, `https://doi.org/10.1016/j.ijrmms.2016.09.013`, 2016.

[19] Favero, V., & Laloui, L.: Impact of CO2 injection on the hydro-mechanical behaviour of a clay-rich caprock, International Journal of Greenhouse Gas Control, 71, 133-141, `https://doi.org/10.1016/j.ijggc.2018.02.017`, 2018.

[20] Hadian, P., & Rezaee, R.: The Effect of Supercritical CO2 on Shaly Caprocks, Energies, 13(1), 149, `https://doi.org/10.3390/en13010149`, 2020.

[21] Hashemi, S. S., & Zoback, M. D.: Permeability evolution of fractures in shale in the presence of supercritical CO2, Journal of Geophysical Research: Solid Earth, 126(8), e2021JB022266, `https://doi.org/10.1029/2021JB022266`, 2021.

[22] Houben, M. E., Desbois, G., & Urai, J. L.: Pore morphology and distribution in the Shaly facies of Opalinus Clay (Mont Terri, Switzerland): Insights from representative 2D BIB–SEM investigations on mm to nm scale, Applied clay science, 71, 82-97., `https://doi.org/10.1016/j.clay.2012.11.006`, 2013.

[23] IPCC: Climate Change 2022: Mitigation of Climate Change, Contribution of Working Group III to the Sixth Assessment Report of the Intergovernmental Panel on Climate Change, Cambridge University Press, Cambridge, UK and New York, NY, USA. `https://doi.org/10.1017/9781009157926`, 2022.

[24] Jia, Y., Lu, Y., Elsworth, D., Fang, Y., & Tang, J.: Surface characteristics and permeability enhancement of shale fractures due to water and supercritical carbon dioxide fracturing, Journal of Petroleum Science and Engineering, 165, 284-297, `https://doi.org/10.1016/j.petrol.2018.02.018`, 2018.

[25] Kivi, I. R., Makhnenko, R. Y., & Vilarrasa, V.: Two-Phase Flow Mechanisms Controlling CO2 Intrusion into Shaly Caprock, Transport in Porous Media, 141(3), 771-798, `https://doi.org/10.1007/s11242-022-01748-w`, 2022.

[26] Li, C., & Laloui, L.: Impact of material properties on caprock stability in CO2 geological storage, Geomechanics for Energy and the Environment, 11, 28-41, `https://doi.org/10.1016/j.gete.2017.06.003`, 2017.

[27] Makhnenko, R. Y., Vilarrasa, V., Mylnikov, D., & Laloui, L.: Hydromechanical aspects of CO2 breakthrough into clay-rich caprock, Energy Procedia, 114, 3219-3228, `https://doi.org/10.1016/j.egypro.2017.03.1453`, 2017.

[28] Marschall, P., Horseman, S., & Gimmi, T.: Characterisation of gas transport properties of the Opalinus Clay, a potential host rock formation for radioactive waste disposal, Oil & gas science and technology, 60(1), 121-139, `https://doi.org/10.2516/ogst:2005008`, 2005.

[29] Menaceur, H., Delage, P., Tang, A. M., & Conil, N.: On the thermo-hydro-mechanical behaviour of a sheared Callovo-Oxfordian claystone sample with respect to the EDZ behaviour, Rock Mechanics and Rock Engineering, 49(5), 1875-1888, `https://doi.org/10.1007/s00603-015-0897-5`, 2016.

[30] Minardi, A., Stavropoulou, E., Kim, T., Ferrari, A., & Laloui, L.: Experimental assessment of the hydro-mechanical behaviour of a shale caprock during CO2 injection, International Journal of Greenhouse Gas Control, 106, 103225, `https://doi.org/10.1016/j.ijggc.2020.103225`, 2021.

[31] Mohajerani, M., Delage, P., Sulem, J., Monfared, M., Tang, A. M., & Gatmiri, B.: The thermal volume changes of the Callovo–Oxfordian claystone, Rock mechanics and rock engineering, 47(1), 131-142, `https://doi.org/10.1007/s00603-013-0369-8`, 2014.

[32] Prakash, R., Nguene, P.C.K., Noshadravan, A., & Abedi, S.: Chemical reactions of carbonate-rich mudstones with aqueous CO2 and their impacts on rock's local microstructural and chemo-mechanical properties, Journal of Natural Gas Science and Engineering, 103, 104587, `https://doi.org/10.1016/j.jngse.2022.104587`, 2022.

[33] Romero, E.: Controlled-suction techniques. 4o Simpósio Brasileiro de Solos Não Saturados. Gehling & F. Schnaid (eds.), Porto Alegre, Brasil, 535-542, 2021.

[34] Rutqvist, J.: The geomechanics of CO2 storage in deep sedimentary formations. Geotechnical and Geological Engineering, 30(3), 525-551, `https://doi.org/10.1007/s10706-011-9491-0`, 2012.

[35] Sciandra, D., Vilarrasa, V., Rahimzadeh Kivi, I., Makhnenko, R., Nussbaum, C., & Rebscher, D.: Coupled HM modeling assists in designing CO2 long-term periodic injection experiment (CO2LPIE) in Mont Terri rock laboratory, In EGU General Assembly Conference Abstracts (pp. EGU21-8982), `https://doi.org/10.5194/egusphere-egu21-8982`, 2021

654 [36] Stamati, O., Andò, E., Roubin, E., Cailletaud, R., Wiebicke, M., et al.: spam: Software for

655 Practical Analysis of Materials, Journal of Open Source Software, Open Journals, 5 (51), pp.2286,

656 `https://doi.org/10.21105/joss.02286`, 2020. .

657 [37] Stavropoulou, E., Andò, E., Roubin, E., Lenoir, N., Tengattini, A., Briffaut, M., & Bésuelle, P.:

658 Dynamics of water absorption in Callovo-Oxfordian claystone revealed with multimodal x-ray

659 and neutron tomography, Frontiers in Earth Science, 8, 6, `https://doi.org/10.3389/feart.`

660 `2020.00006`, 2020

661 [38] Stavropoulou, E., & Laloui, L.: Evaluating CO2 breakthrough in a shaly a caprock material:

662 a multi-scale experimental approach. Scientific Reports, 12(1), 1-19, `https://doi.org/10.`

663 `1038/s41598-022-14793-8`, 2022.

664 [39] Vego, I., Tengattini, A., Andò, E., Lenoir, N., & Viggiani, G.: Effect of high relative humidity

665 on a network of a water-sensitive particles (couscous) as revealed by in-situ x-ray tomography,

666 Soft Matter, `https://doi.org/10.1039/D2SM00322H`, 2022.

667 [40] Viggiani, G., & Hall, S. A.: Full-field measurements, a new tool for laboratory experimental

668 geomechanics, In Proceedings of the 4th Symposium on Deformation Characteristics of Geoma-

669 terials, 1, 3-26, 2008.

670 [41] Viggiani, G., Andò, E., Takano, D., & Santamarina, J. C.: Laboratory X-ray tomography: a

671 valuable experimental tool for revealing processes in soils, Geotechnical Testing Journal, 38(1),

672 61-71, `https://doi.org/10.1520/GTJ20140060`, 2015.

673 [42] Vilarrasa, V., Carrera, J., Olivella, S., Rutqvist, J., & Laloui, L.: Induced seismicity in geologic

674 carbon storage, Solid Earth, 10(3), 871-892, `https://doi.org/10.5194/se-10-871-2019`,

675 2019.

676 [43] Voltolini, M., & Ajo-Franklin, J. B.: The sealing mechanisms of a fracture in opalinus clay

677 as revealed by in situ synchrotron x-ray micro-tomography, Frontiers in Earth Science, 8, 207,

678 `https://doi.org/10.3389/feart.2020.00207`, 2020.

679 [44] Wang, L. L., Bornert, M., Chanchole, S., Yang, D. S., Héripré, E., Tanguy, A., & Calde-

680 maison, D.: Micro-scale experimental investigation of the swelling anisotropy of the Callovo-

681   Oxfordian argillaceous rock, Clay Minerals, 48(2), 391-402, `https://doi.org/10.1180/`
682   `claymin.2013.048.2.17`, 2013.

683 [45] Wang, S., & Tokunaga, T. K.: Capillary pressure–saturation relations for supercritical CO2 and
684   brine in limestone/dolomite sands: Implications for geologic carbon sequestration in carbonate
685   reservoirs, Environmental science & technology, 49(12), 7208-7217, `https://doi.org/10.`
686   `1021/acs.est.5b00826`, 2015.

687 [46] Wollenweber, J., Alles, S., Busch, A., Krooss, B. M., Stanjek, H., & Littke, R.: Experimental
688   investigation of the CO2 sealing efficiency of caprocks, International Journal of Greenhouse Gas
689   Control, 4(2), 231-241, `https://doi.org/10.1016/j.ijggc.2010.01.003`, 2010.

690 [47] Yang, K., Zhou, J., Xian, X., Zhou, L., Zhang, C., Tian, S., Lu, Z., & Zhang, F.: Chemical-
691   mechanical coupling effects on the permeability of shale subjected to supercritical CO2-water
692   exposure, Energy, 248, 123591, `https://doi.org/10.1016/j.energy.2022.123591`, 2022.

693 [48] Yasuhara, H., Kinoshita, N., Ohfuji, H., Lee, D. S., Nakashima, S., & Kishida, K.: Tem-
694   poral alteration of fracture permeability in granite under hydrothermal conditions and its in-
695   terpretation by coupled chemo-mechanical model, Applied Geochemistry, 26(12), 2074-2088,
696   `https://doi.org/10.1016/j.apgeochem.2011.07.005`, 2021.

697 [49] Zappone, A., Rinaldi, A. P., Grab, M., Wenning, Q. C., Roques, C., Madonna, C., Obermann,
698   A. C., Bernasconi, S. M., Brennwald, M. S., Kipfer, R., Soom, F., Cook, P., Guglielmi, Y.,
699   Nussbaum, C., Giardini, D., Mazzotti, M., & Wiemer, S.: Fault sealing and caprock integrity for
700   CO2 storage: an in situ injection experiment, Solid Earth, 12, 319–343, `https://doi.org/10.`
701   `5194/se-12-319-2021`, 2021.